Additive Manufacturing: Metallurgy, Cut Analysis & Porosity

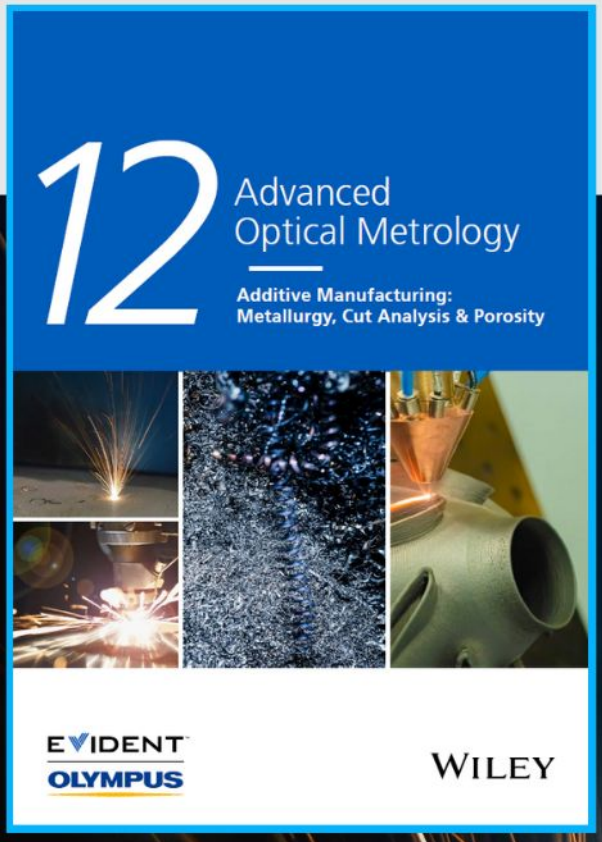

The latest eBook from Advanced Optical Metrology. Download for free.

In industry, sector after sector is moving away from conventional production methods to additive manufacturing, a technology that has been recommended for substantial research investment.

Download the latest eBook to read about the applications, trends, opportunities, and challenges around this process, and how it has been adapted to different industrial sectors.

EVIDENT
OLYMPUS

WILEY

ADVANCED FUNCTIONAL MATERIALS
www.afm-journal.de

On the Origin of Seebeck Coefficient Inversion in Highly Doped Conducting Polymers

Kai Xu, Tero-Petri Ruoko, Morteza Shokrani, Dorothea Scheunemann, Hassan Abdalla, Hengda Sun, Chi-Yuan Yang, Yuttapoom Puttisong, Nagesh B. Kolhe, José Silvestre Mendoza Figueroa, Jonas O. Pedersen, Thomas Ederth, Weimin M. Chen, Magnus Berggren, Samson A. Jenekhe, Daniele Fazzi, Martijn Kemerink,* and Simone Fabiano**

A common way of determining the majority charge carriers of pristine and doped semiconducting polymers is to measure the sign of the Seebeck coefficient. However, a polarity change of the Seebeck coefficient has recently been observed to occur in highly doped polymers. Here, it is shown that the Seebeck coefficient inversion is the result of the density of states filling and opening of a hard Coulomb gap around the Fermi energy at high doping levels. Electrochemical n-doping is used to induce high carrier density (>1 charge/monomer) in the model system poly(benzimidazobenzophenanthroline) (BBL). By combining conductivity and Seebeck coefficient measurements with in situ electron paramagnetic resonance, UV–vis–NIR, Raman spectroelectrochemistry, density functional theory calculations, and kinetic Monte Carlo simulations, the formation of multiply charged species and the opening of a hard Coulomb gap in the density of states, which is responsible for the Seebeck coefficient inversion and drop in electrical conductivity, are uncovered. The findings provide a simple picture that clarifies the roles of energetic disorder and Coulomb interactions in highly doped polymers and have implications for the molecular design of next-generation conjugated polymers.

1. Introduction

Because of their tunable electrical and optical properties, ease of fabrication, flexible and biocompatible nature,[1] semiconducting polymers are well suited for numerous opto- and bioelectronic applications, including organic light-emitting diodes,[2] organic solar cells,[3] batteries/supercapacitors,[4] thermoelectrics,[5] (bio-)sensors,[6] and neuromorphic circuits.[7] For all these applications, tuning the electrical conductivity of the semiconducting polymers via oxidative (p-type) or reductive (n-type) doping enables the optimization of the electronic device's performance and the emergence of new properties.[8] This is typically achieved by adding molecular[9] or polymeric[10] dopants that act as either electron acceptors or donors when mixed with the conjugated polymer, thus tuning the polymer's charge carrier density and

K. Xu,[+] T.-P. Ruoko,[++] H. Sun,[+++] C.-Y. Yang, M. Berggren, S. Fabiano
Laboratory of Organic Electronics
Department of Science and Technology
Linköping University
Norrköping SE-60174, Sweden
E-mail: simone.fabiano@liu.se

The ORCID identification number(s) for the author(s) of this article can be found under https://doi.org/10.1002/adfm.202112276.

© 2022 The Authors. Advanced Functional Materials published by Wiley-VCH GmbH. This is an open access article under the terms of the Creative Commons Attribution License, which permits use, distribution and reproduction in any medium, provided the original work is properly cited.

[+]Present address: State Key Laboratory of Metastable Materials Science and Technology, Yanshan University, Qinhuangdao 066004, China
[++]Present address: Smart Photonic Materials, Faculty of Engineering and Natural Sciences, Tampere University, Tampere 33720, Finland
[+++]Present address: State key Laboratory for Modification of Chemical Fibers and Polymer Materials, Donghua University, Shanghai 201620, China
[++++]Present address: Università di Bologna, Dipartimento di Chimica "Giacomo Ciamician", via F. Selmi 2, Bologna 40126, Italy

DOI: 10.1002/adfm.202112276

M. Shokrani, D. Scheunemann, M. Kemerink
Center for Advanced Materials
Heidelberg University
69120 Heidelberg, Germany
E-mail: martijn.kemerink@cam.uni-heidelberg.de

H. Abdalla, Y. Puttisong, W. M. Chen, M. Kemerink
Division of Electronics and Photonic Materials
Department of Physics, Chemistry and Biology
Linköping University
Linköping SE-58183, Sweden

N. B. Kolhe, S. A. Jenekhe
Department of Chemical Engineering and Department of Chemistry
University of Washington
Seattle, WA 98195, USA

J. S. M. Figueroa, J. O. Pedersen, T. Ederth
Division of Biophysics and Bioengineering
Department of Physics, Chemistry and Biology
Linköping University
Linköping SE-58183, Sweden

M. Berggren, S. Fabiano
Wallenberg Wood Science Center
Linköping University
Norrköping SE-60174, Sweden

 © 2022 The Authors. Advanced Functional Materials published by Wiley-VCH GmbH

16163028, 2022, 20, Downloaded from https://onlinelibrary.wiley.com/doi/10.1002/adfm.202112276 by Area Sistemi Dipart & Document, Wiley Online Library on [23/11/2022]. See the Terms and Conditions (https://onlinelibrary.wiley.com/terms-and-conditions) on Wiley Online Library for rules of use; OA articles are governed by the applicable Creative Commons License

16163028, 2022, 20, Downloaded from https://onlinelibrary.wiley.com/doi/10.1002/adfm.202112276 by Area Sistemi Dipart & Document, Wiley Online Library on [23/11/2022]. See the Terms and Conditions (https://onlinelibrary.wiley.com/terms-and-conditions) on Wiley Online Library for rules of use; OA articles are governed by the applicable Creative Commons License

electrical conductivity. Electrochemical doping is another effective way of tuning the electrical and optical properties of conjugated polymers.[11] In electrochemical doping, the polymer film is oxidized/reduced by injection of electronic charges from the working electrode, which are compensated by the insertion of counterions from the electrolyte.[12]

Tuning the electronic properties of semiconducting polymers via doping is especially important for organic thermoelectric applications. In thermoelectrics, the figure of merit that quantifies the energy-to-electricity transduction is ZT, which is proportional to both the electrical conductivity (σ) and Seebeck coefficient (S). The latter depends on the energy distribution of mobile charge carriers relative to the Fermi level (E_F). Since electronic doping of organic semiconductors typically decreases S while simultaneously increasing σ, the power factor ($S^2\sigma$) and ZT usually reach their maximum values at intermediate doping levels. The sign of S is often used to determine the polarity of the majority charge carriers in organic semiconductors. However, in recent years a change in the sign of S has sometimes been observed to occur in highly doped semiconducting polymers. This observation is significant since it could enable complete thermoelectric modules with n-type and p-type legs made from the same polymer-dopant system at different doping levels. For example, Hwang et al.[13] observed that poly(pyridinium phenylene) doped with sodium naphthalenide undergoes a conductor to insulator transition and associated sign change in the Seebeck coefficient when the doping level is larger than one electron per repeating unit (eru). Liu et al.[14] observed later a similar change in the sign of S when doping the naphthalenediimide-based polymer bearing glycolated side chains (PNDI2TEG-2T) with the benzimidazole-based dopant N-DMBI at a dopant concentration of 42 mol%, although this inversion was not associated with a decrease in conductivity. More recently, Liang et al.[15] studied the sign inversion of eight different p-type polymers that were highly doped with $FeCl_3$ or $NOBF_4$ molecular dopants. In their case, the inversion from p-type to n-type conduction was associated with a coinciding decrease in electrical conductivity, especially for those polymers that exhibited a large negative S at the highest doping levels. Hall measurements performed on these highly doped polymeric systems suggested that the majority charge carriers changed from holes to electrons in those polymers exhibiting the largest inversion in S. The inversion only occurred at extremely high doping levels surpassing 2 eru and was attributed to the formation of a delocalized transport band for electrons in the crystalline regions of the polymers. However, their results leave it open whether the inversion of the Seebeck coefficient is determined by other factors, such as the dopant-induced energetic disorder that accompanies high carrier densities.

Here, we demonstrate that the inversion of the Seebeck coefficient and drop in the electrical conductivity at a high doping level is caused by the filling of the density of states (DOS) and the opening of a hard Coulomb gap around the Fermi energy. We used electrochemical doping to fine-tune the doping level of the n-type polymer model system poly(benzimidazobenzophenanthroline) (BBL) from 0 to 1.5 eru. We chose BBL as an example of rigid mixed ion-electron conducting polymers that can sustain a high degree of chemical[10b,16] and electrochemical[17] doping with excellent stability in ambient and no degradation of the electrical performance.[17a] By combining electrical and electrochemical characterization with in situ electron paramagnetic resonance (EPR), UV–vis–NIR, and Raman spectroelectrochemistry, as well as density functional theory (DFT) calculations, we report the formation of multiply charged species with reduced mobility as the doping level passes 0.7 eru. Kinetic Monte Carlo simulations show that double occupation and Coulomb interactions occurring at high doping level cause the opening of a hard Coulomb gap in the density of states of the system, which is responsible for the sign change of S. We also found that the previously proposed soft Efros–Shklovskii (ES) Coulomb gap[14] does not affect the sign of S, while both hard and soft Coulomb gaps are responsible for the reduction in the electrical conductivity observed at high doping level. Our results provide an explanation for the trends of conductivity and Seebeck coefficient observed in highly doped conjugated polymers and suggest a guideline for the rational design of next-generation organic thermoelectric materials, with the attention being shifted back from a microstructural level to a molecular level.

2. Results and Discussion

2.1. Electrochemical Doping of BBL

In situ conductivity measurements of BBL were performed using an organic electrochemical transistor (OECT) setup (**Figure 1**A). In brief, source and drain electrodes (3 nm Cr and 30 nm Au) were deposited on a glass substrate, followed by spin-coating of a 60 nm thick BBL layer. A water-based sodium poly(styrenesulfonate) (PSSNa) gel electrolyte[18] was cast on top of the BBL film, and an Ag/AgCl pellet was immersed into the electrolyte and used as the gate electrode. The chemical structures of BBL and PSSNa are illustrated in Figure 1B. To facilitate the in situ conductivity measurements, the OECTs had a large channel length (0.5 mm) while the channel width was 10 mm. Because of the large active area, during characterization we allowed enough time for the ions to fully penetrate into the film after applying a gate voltage (V_G). The electrical characteristics of the BBL-based OECTs are illustrated in Figure S1 in the Supporting Information. In the gate voltage range –0.1 to 0.5 V (n-type gating), the devices show typical n-type output and transfer electrical characteristics. However, as the gate voltage is increased further, the drain current (I_D) onset shifts to higher drain voltages (V_D). In order to measure the conductivity of the OECT channel, a small voltage of 10 mV was applied between the source and drain terminals. Since in this case V_G is much larger than V_D, we assume a uniformly reduced BBL throughout the channel plane. The conductivity of BBL under different gate voltages is shown in Figure 1C and Figure S2A in the Supporting Information. The conductivity first increases

M. Berggren, S. Fabiano
n-Ink AB
Teknikringen 7, Linköping SE-58330, Sweden
D. Fazzi[++++]
Institute of Physical Chemistry
University of Cologne
50939 Cologne, Germany
E-mail: daniele.fazzi@unibo.it

© 2022 The Authors. Advanced Functional Materials published by Wiley-VCH GmbH

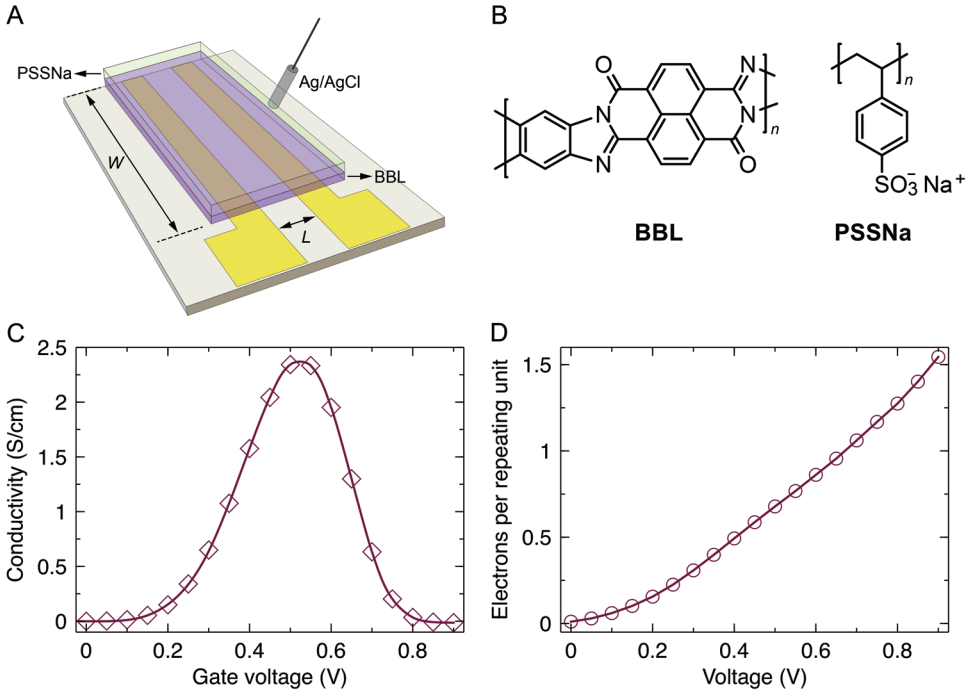

Figure 1. BBL-based n-type organic electrochemical transistor. A) Schematic structure of the organic electrochemical transistor; width and length of the channel are 10 and 0.5 mm, respectively. B) Chemical structures of poly(benzimidazobenzophenanthroline) (BBL) and sodium poly(4-styrenesulfonate) (PSSNa), which were used as the channel semiconducting polymer and water-based gate electrolyte. C) Conductivity of the BBL layer measured using $V_D = 0.01$ V. D) Electrons per repeating unit inside the BBL channel.

with higher gate voltages due to electrochemical doping of the BBL film, with more cations penetrating into the BBL film from the electrolyte to maintain charge neutrality in the reduced BBL film. The conductivity of BBL reaches a maximum of 3.1 S cm^{-1} at 0.46 V (Figure S2A, Supporting Information), followed by decreasing conductivity at higher gate voltages. BBL becomes nearly nonconductive at gate voltages larger than 0.6 V, with the negative conductivity values resulting from leakage of the gate current (Figure S1, Supporting Information).

To determine the degree of electrochemical doping in BBL, we reduced the gate leakage current by allowing the PSSNa gel electrolyte to partially dry under ambient conditions from 40 to 12 wt% water content. This reduced the gate leakage current from 0.54 to 0.042 μA at $V_G = 0.6$ V, as shown in Figure S1C,D in the Supporting Information. However, the drying of the gel also significantly reduces the OECT switching speed. To compensate for the slower response time, we allowed the OECT to stabilize for an extended period of time ($t = 2700$ s) at the set gate voltage before performing steady-state electrical characterization. The larger electrolyte resistance shifts the maximum drain current toward higher gate voltages by 50 mV and results in a slight decrease in conductivity (from 3.1 to 2.3 S cm^{-1} at maximum), as shown in Figure S2A in the Supporting Information. Thus, we anticipate that the charged states of BBL at a specific potential remain essentially unchanged. The greatly reduced leakage gate current allows us to determine the electron density within the BBL channel by integrating the transferred gate current, as shown in Figure S2B–D in the Supporting Information. The electron density was further used to calculate the number of electrons per repeating unit (eru), as shown in Figure 1D. The number of charges in the BBL channel increases with the applied voltage, suggesting that the drop in conductivity at high gate voltages is due to a reduction in electron mobility. The gate voltage at which the conductivity begins to decrease coincides with BBL reaching a doping degree of 0.7 eru.

2.2. In Situ Electron Paramagnetic Resonance

We then performed in situ EPR[19] to detect unpaired charge carriers in the electrochemically doped BBL thin films. To this end, a 20 nm thick gold layer was deposited on a PET substrate, followed by deposition of the 60 nm thick BBL layer. To minimize the microwave losses, a thin PSSNa gel layer was cast on top of the BBL film, while the Ag/AgCl pellet gate electrode was placed outside the resonance chamber. The EPR spectra under different gate voltages are shown in **Figure 2**A. While pristine BBL shows no EPR signal,[10a] electrochemically doped BBL shows a strong EPR signal that increases with gate voltage. The integrated total spin count at different applied voltages increases until saturating at around 0.4–0.5 V (Figure 2B). Saturation of the total spin density indicates multiply charged states forming in BBL once the doping level passes 0.5 eru. In agreement with the density functional theory calculations reported below, these multiply charged states are EPR active, resulting in the spin density remaining high despite the decrease in conductivity at $V > 0.6$ V. Further doping leads to increased formation of multiply charged states that have a spinless ground state character. This reduces the effective number of singly occupied orbital states that are EPR-active and thus results in a reduction

© 2022 The Authors. Advanced Functional Materials published by Wiley-VCH GmbH

16163028, 2022, 20, Downloaded from https://onlinelibrary.wiley.com/doi/10.1002/adfm.202112276 by Area Sistemi Dipart & Document, Wiley Online Library on [23/11/2022]. See the Terms and Conditions (https://onlinelibrary.wiley.com/terms-and-conditions) on Wiley Online Library for rules of use; OA articles are governed by the applicable Creative Commons License

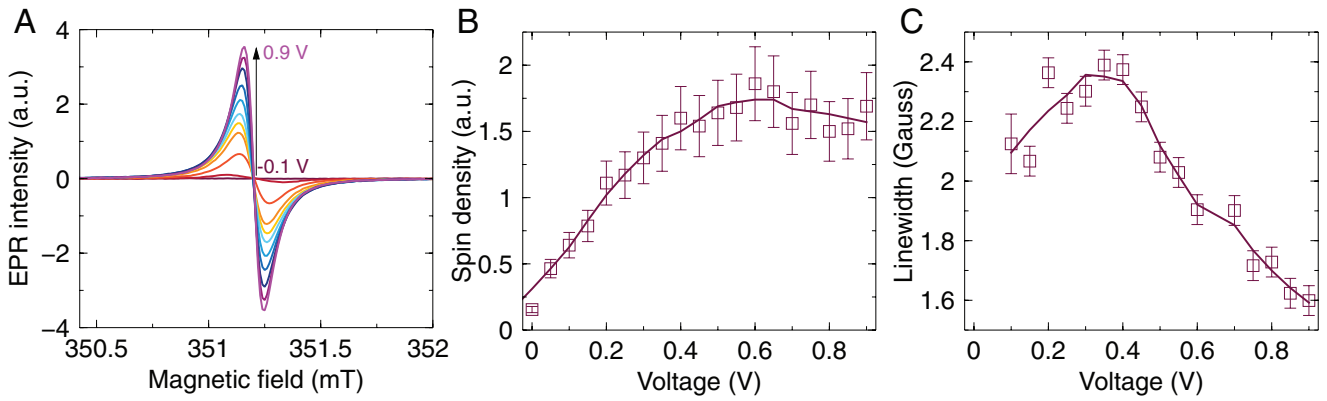

Figure 2. Voltage dependent in situ EPR spectroscopy. A) EPR spectra, B) EPR spin density, and C) EPR linewidth under different applied voltages.

in the effective spin count. Interestingly, the EPR linewidth at different gate voltages initially increases until about 0.35 V applied voltage, followed by a drop as the voltage increases beyond 0.4 V (Figure 2C).

We can correlate the EPR linewidth to both eru (Figure 1D) and conductivity (Figure 1C). The EPR linewidth is generally ascribed to both intrinsic and extrinsic contributions.[20] In the former case, the linewidth is of Lorentzian type and is dictated by spin relaxation. The latter case is typically ascribed to the dynamic interactions of the unpaired electrons with the spin environment, leading to deviations from the Lorentzian lineshape.[20–21] In the range 0–0.4 V the EPR linewidth deviates from the Lorentzian lineshape. Considering that polarons are highly mobile within this range (i.e., high conductivity at voltages <0.5 V), one could expect an increase in spin scattering events, both between polarons and the nuclear spin environment and between spin-unpaired polarons. Increased spin scattering events can thus explain the increasing EPR linewidth. Such interactions are statistical in nature and lead to non-Lorentzian type line broadening effects.[20–21] In the range 0.4–0.9 V, the system reaches eru > 1 with a drastic drop in the electrical conductivity. Here, the polarons become increasingly immobile, leading to a reduced number of spin scattering events and the EPR linewidth narrows due to longer relaxation times. This is indeed reflected in our results that show a nearly perfect Lorentzian lineshape at 0.4 V (Figure S3, Supporting Information) The linewidth continuously becomes narrower beyond 0.4V with a Lorentzian lineshape, and we ascribe this to the reduction of spin dephasing time due to the increasing charge carrier localization.

2.3. UV–vis Spectroelectrochemistry

Next, we characterize the optical properties of the electrochemically doped BBL films. The difference UV–vis spectra of electrochemically doped BBL measured in reflectance mode are shown in **Figure 3**A,B. The full 375–1950 nm range spectra are shown in Figure S4 in the Supporting Information along with the normalized absorption spectra of pristine and tetrakis(dimethylamino)ethylene (TDAE)-doped BBL films. As BBL is reduced at higher applied voltages, the UV–vis absorption bands of charged species in BBL appear along with a bleaching of the BBL ground-state absorption. The difference absorption spectrum obtained by electrochemical doping of BBL bears a striking resemblance with that obtained via chemical doping of BBL with TDAE (Figure S4C, Supporting Information), confirming that the changes in absorption are a result of negatively charged polaronic species in BBL.[16]

The different spectra of electrochemically doped BBL shown in Figure 3 have two voltage ranges with different spectral signatures, as illustrated in the absorption intensity versus applied voltage curves at select wavelengths shown in Figure S5 in the Supporting Information. We first focus on the wavelength range 650–1100 nm (Figure 3B). When the voltage is first applied, two overlapping absorption bands assigned to low spin density BBL appear around 725 and 875 nm. Both absorptions grow until the applied voltage reaches 0.5 V. When the voltage is increased further, the 875 nm absorption decreases rapidly. The 725 nm absorption decreases slightly between 0.6 and 0.7 V due to an overlap of the two absorption bands but increases again at higher applied voltages. This indicates that the 875 nm absorption band is characteristic of low spin density BBL, whereas the 725 nm absorption band is observed for both low and high spin density (i.e., multiply charged) species. Next, we turn to the differential absorption in the range 375–700 nm (Figure 3A). When the gate voltage is first applied, a positive absorption band appears at 410 nm along with an extended ground state bleach visible as a negative difference absorption between 455 and 675 nm. However, the shape of the bleach does not directly match with the ground state absorption of pristine BBL presented in Figure S4B in the Supporting Information. This indicates that some positive polaronic absorption bands also overlap with the ground state absorption, distorting the shape of the bleach. In the voltage range up to 0.5 V two isosbestic points are visible at 455 and 675 nm, indicating a direct conversion of pristine BBL to the charged form. At larger applied voltages, an intense positive absorption band forms at 480 nm. Based on the electrical characterization and EPR results discussed above, we assign the band at 480 nm to the absorption of multiply charged (high spin density) BBL. The negative ground state bleach also grows in intensity and more closely mirrors the absorption spectrum of pristine BBL, indicating that the overlapping polaronic absorption bands associated with singly charged BBL disappear at larger voltages.

© 2022 The Authors. Advanced Functional Materials published by Wiley-VCH GmbH

16163028, 2022, 20, Downloaded from https://onlinelibrary.wiley.com/doi/10.1002/adfm.202112276 by Area Sistemi Dipart & Document, Wiley Online Library on [23/11/2022]. See the Terms and Conditions (https://onlinelibrary.wiley.com/terms-and-conditions) on Wiley Online Library for rules of use; OA articles are governed by the applicable Creative Commons License

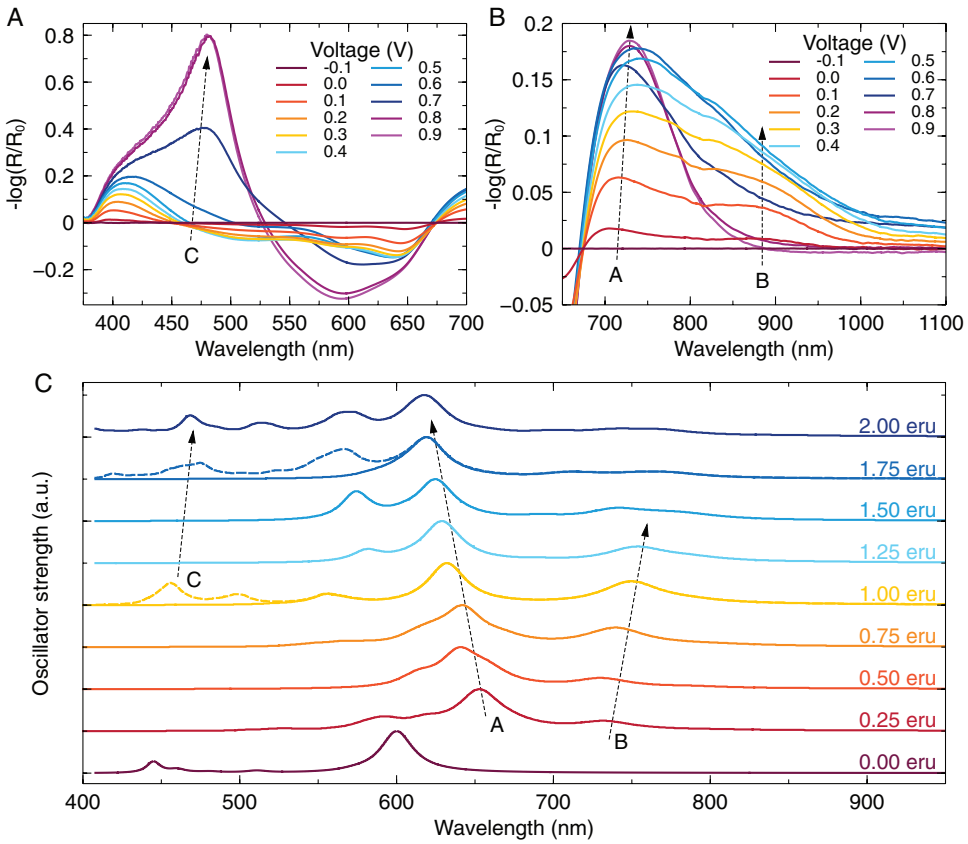

Figure 3. UV–vis spectroscopy. In situ difference UV–vis spectra of BBL measured in reflectance mode in the ranges of A) 375–700 nm and B) 650–1100 nm. The baseline measurement was the same BBL film kept at –0.1 V applied voltage (straight line) to dedope the film prior to measuring the difference spectra. UV–vis measurements were performed of BBL films on top of gold covered glass substrates with doctor bladed PSSNa electrolyte and the Ag/AgCl pellet gate electrode positioned away from the illuminated area. C) Computed TD-DFT electronic transitions (wB97X-D/6-31G*) for pristine (0.00 eru) and charged species (0.25–2.00 eru). Relevant electronic transitions, as discussed in the main text, are labeled A, B, and C. TD-DFT vertical energies were shifted by 0.4 eV, and the linear spectra were computed as a Lorentzian convolution of transition energies with a full-width half-maximum of 0.1 eV. Dotted lines for the cases 1.00 and 1.75 eru represent TD-DFT calculations where more than 300 excited states were computed.

2.4. DFT Calculations

To get insight into the electrochemical doping processes occurring in BBL, we modeled both the pristine and charged states of the polymer via DFT calculations (see details in the Supporting Information and ref. [22]). An oligomer featuring four repeat units (BBL_4) was considered as a model system for the polymer chain. The neutral electronic state (i.e., 0 eru) is representative of the pristine state. Differently charged states of BBL_4 correspond to various doping levels induced by increasing the applied voltage. Charged states, together with their different spin-state multiplicities (see the Supporting Information), varying from 1 to 8 electrons on BBL_4 (equivalent to 0.25 to 2 eru) were considered. The computed electronic transitions at the time-dependent-DFT (TD-DFT) level are reported in Figure 3C. For the charged species corresponding to 0.25 eru (previously identified as a polaron), TD-DFT calculations show dipole active electronic transitions at lower energies than the optical gap of the neutral state (≈600 nm), namely an intense band (labeled as A) and a weaker band at even lower energy (labeled as B). Bands A and B correspond to electronic transitions between the ground and excited states of the charged species, involving singly occupied/unoccupied frontier molecular orbitals. Despite the well-known limits of a TD-DFT treatment, i.e., lack of (static) electron correlation effects[22–23] as well as underestimation of the charge transfer and diffuse valence excited state energies, we can qualitatively assign the experimentally observed optical features.

We assigned the transitions A and B of the 0.25 eru charged species to the observed bands in the NIR region at 725 and 875 nm for a voltage of 0.1 V, respectively (Figure 3B). By increasing the number of electrons per repeat unit from 0.25 to 1 eru, both bands increase in oscillator strength. A similar trend for the intensities can be observed in the experimental NIR spectra: both the intensities of the 725 nm A) and 875 nm B) bands increase when the voltage rises from 0.1 to 0.2 V (≈0.25 eru) up to 0.6 V (≈1 eru). Starting at 0.7 V (≈1.25 eru), the intensity of band B decreases and vanishes at 0.9 V (≈1.5 eru). We observed an equivalent behavior for the computed TD-DFT transitions of multiply charged species: starting at 1.25 eru, the intensity of band B decreases with respect to band A and then vanishes at 2 eru. Furthermore, band A gradually blue shifts, becoming narrower at 2 eru. Given these trends in the NIR spectral region we can suggest a possible correlation between

© 2022 The Authors. Advanced Functional Materials published by Wiley-VCH GmbH

16163028, 2022, 20, Downloaded from https://onlinelibrary.wiley.com/doi/10.1002/adfm.202112276 by Area Sistemi Dipart & Document, Wiley Online Library on [23/11/2022]. See the Terms and Conditions (https://onlinelibrary.wiley.com/terms-and-conditions) on Wiley Online Library for rules of use; OA articles are governed by the applicable Creative Commons License

16163028, 2022, 20, Downloaded from https://onlinelibrary.wiley.com/doi/10.1002/adfm.202112276 by Area Sistemi Dipart & Document, Wiley Online Library on [23/11/2022]. See the Terms and Conditions (https://onlinelibrary.wiley.com/terms-and-conditions) on Wiley Online Library for rules of use; OA articles are governed by the applicable Creative Commons License

the applied voltages and the induced charged states in BBL. At low voltages (0.1–0.2 V), the charged species corresponds to 0.25 eru, showing two polaronic transitions, bands A (725 nm) and B (875 nm). At 0.6–0.7 V, the doping level reaches 1 eru, and the two bands reach their maximum intensities. From 0.7 to 0.8 V, the doping level increases from 1.25 eru (0.8 V) to 1.5–2 eru (0.9 V), leading to one prominent absorption band (band A) in the NIR region.

To verify if intense absorptions appear also in the 450–500 nm wavelength range, as observed experimentally, see the broad and intense band appearing at 480 nm for $V > 0.6$ V (Figure 3A), we performed TD-DFT calculations by including a large number of excited states (>300) only for specific multiply charged species (i.e., 1.00, 1.75, and 2.00 eru). TD-DFT calculations indeed confirm the presence of intense dipole allowed transitions in the 450–500 nm range (see band C in Figure 3C) for the multiply charges species 1.00, 1.75, and 2.00 eru, in qualitative agreement with the experimental observations. However, a note of caution should be given: considering the composition of the TD-DFT excited state wavefunction (i.e., a large number of singly occupied/unoccupied molecular orbitals with small expansion coefficients) and the fractional occupation number weighted density (FOD) analysis,[24] suggesting strong static correlation effects for multicharged species,[22b] we believe that the TD-DFT description can only be used to suggest a qualitative correlation with the experiments. Notably, as for the case of the low-energy NIR spectral range (600–900 nm), also in the 450–500 nm wavelength window our TD-DFT calculations support the interpretation of multicharged high-spin states induced at voltages above 0.6 to 0.7 V.

Taken together, the in situ UV–vis spectroscopy and TD-DFT calculations indicate that pristine BBL is initially reduced into a singly charged polaronic state (low spin density, 0.25 eru) at low gate voltages, reaching up to 1 eru for voltages approaching 0.6 to 0.7 V. An increase in the voltage up to 0.8–0.9 V leads to two intense UV–vis bands (≈470 and ≈750 nm) assigned to multicharged species featuring more than 1.75 eru (high spin density). Importantly, the UV–vis experiments and TD-DFT calculations allow the conclusion that the conductivity maximum is reached before 1 eru.

2.5. Raman Spectroscopy

Next, we turn to Raman spectroscopy to elucidate how the molecular and electronic structures change upon electrochemical doping. The Raman spectra in the extended 250–2000 cm^{-1} range are shown in Figure S6 in the Supporting Information, with close-up spectra of the weaker vibrational modes shown in Figure S7 in the Supporting Information. The most evident sign of polaron formation in BBL is a decrease in the Raman intensity in almost the whole measurement range. The most intense Raman modes are shown in **Figure 4**A. The modes visible for undoped pristine BBL are located at w_1 = 1705 cm^{-1}, w_3 = 1592 cm^{-1}, w_4 = 1529 cm^{-1}, and w_5 = 1384 cm^{-1}. In the experimental Raman spectra, all pristine peaks gradually decrease in intensity with larger applied voltages, reaching a minimum by 0.4–0.5 V. No Raman modes close to w_1 and w_4 are visible at higher applied voltages. On the other hand, a significant increase at voltages larger than 0.4 V is observed for w_5 along with a gradual shift toward slightly lower energy at $w_{5'}$ = 1360 cm^{-1}. Interestingly, w_3 increases again between 0.4 and 0.7 V while shifting slightly to 1598 cm^{-1}, only to decrease again at even larger applied voltages. Starting from 0.6 to 0.7 V a new vibrational mode appears at w_2 = 1648 cm^{-1}.

The variations in frequencies and intensities of the experimental Raman spectra upon electrochemical doping can be correlated with the DFT calculations of charged states. The computed Raman spectra for the neutral (0 eru) and multicharged (0.25–2 eru) states of BBL_4 are reported in Figure 4B. Generally, DFT spectra correctly predict the vibrational transitions and intensity changes in the Raman spectra upon doping, even though some intensity patterns and relative ratios (e.g., see peaks around 1529 and 1384 cm^{-1}) could not be adequately described, even for the undoped pristine case. Such behavior is expected and can be traced back to the quasi resonance conditions the experimental spectra were recorded at. According to the Albrecht theory of Raman intensities,[25] (quasi) resonance conditions between the excitation laser and the electronic transitions of the system dramatically affect the Raman intensities of those normal modes, which are vibronically coupled with the excited states. Our computed DFT Raman spectra, on the contrary, refer to out-of-resonance conditions, and as such, the intensity pattern of some normal modes may differ from the experimental data.[26] Besides some resonance effects, which cannot be properly described at this level of theory, most of the Raman transitions and intensity variations can be clearly assigned.

For the pristine state (0 eru, corresponding to 0.0–0.1 V), we can do the following assignments between theoretical and experimental in situ Raman spectra: w_1 at 1705 cm^{-1} (Figure 4B) is the symmetric C=O stretching mode, w_3 at 1598 cm^{-1} is the C=C/C−C breathing of the naphthalene ring, and w_4 (1529 cm^{-1}) and w_5 (1384 cm^{-1}) are linear combinations of C−N and C−C stretchings. Upon charging, starting with the 0.25 eru species, a new weak Raman transition appears. This peak, labeled w_2, corresponds to the symmetric C=O stretching mode localized on the polymer repeat unit upon which the charge relaxes (i.e., polaron unit).[22] This transition is not visible in the experimental Raman spectrum recorded at 0.1 V because of its very low intensity. By increasing the number of electrons per repeat unit (i.e., doping level), w_1 decreases in intensity while w_2 gradually increases. Notably, passing from 0.75 to 1.00 eru species, w_1 disappears and w_2 gets significantly enhanced. Furthermore, within the 0.75–1.00 eru range, w_4 and w_5 peaks disappear and two new peaks, named $w_{4'}$ and $w_{5'}$, increase in intensity. Moving from 1.00 to 1.75 eru, w_2 preserves its intensity, and w_4 and w_5 intensities further increase.

These trends are well correlated with the experimental in situ voltage dependent Raman spectra. w_2 can be assigned to the observed peak at 1648 cm^{-1}, which appears around 0.6–0.7 V. This voltage range, as observed previously for the UV–vis–NIR spectra, corresponds to the 0.75–1.00 eru species. w_2 intensity increases up to 0.9 V, corresponding to the predicted DFT trend between 1.5 and 1.75 eru. Similarly, we assigned the decrease in the w_4 peak intensity between 0.75 and 1.00 eru to the disappearance of the 1529 cm^{-1} peak at around 0.6–0.7 V. At the same time, the disappearance of w_5 and the growth of $w_{5'}$ peak

© 2022 The Authors. Advanced Functional Materials published by Wiley-VCH GmbH

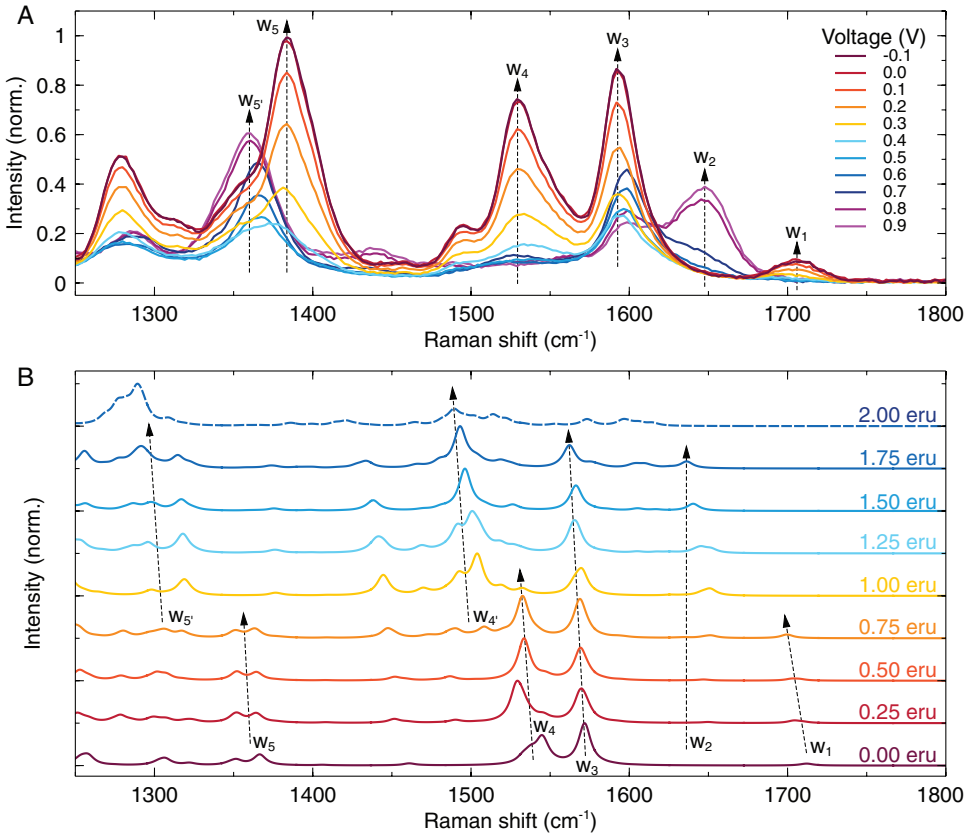

Figure 4. Raman spectroscopy. A) In situ Raman spectra of BBL with 532 nm excitation in the range 1250–1800 cm^{-1}. The spectra are scaled relative to the normalized w_1 band for $V = -0.1$ V. Raman measurements were performed of BBL films on top of gold covered glass substrates with doctor bladed PSSNa electrolyte and the Ag/AgCl pellet gate electrode positioned away from the illuminated area. B) Normalized computed out-of-resonance DFT Raman spectra (wB97X-D/6-31G*) for pristine (0.00 eru) and multicharged species (0.25–2.00 eru). Relevant Raman modes, as discussed in the main text, are labeled as w_i (i = 1–5). DFT frequencies were linearly scaled by a factor of 0.93.

between 0.50 and 0.75 eru can be attributed to the observed Raman active transition at 1360 cm^{-1} starting at 0.4–0.5 V. The computed $w_{4'}$ Raman active mode, which becomes prominent starting at 1.00 eru, is however, not observed in the in situ Raman spectra. We believe that in this region (1500–1600 cm^{-1}) quasi resonance effects are predominant so that the computed (out-of-resonance) Raman pattern might not find an experimental counterpart. Yet, we can assign the major changes in the Raman spectra upon charging, precisely correlating the voltage-dependent spectra to the computed multiply charged species. The Raman analysis confirms and further strengthens the correlations we previously drew for the UV–vis–NIR spectra: i) at 0.1 V the active charged species is the 0.25 eru; ii) by increasing the voltage up to 0.6–0.7 V the doping level increases up to 0.75–1.00 eru, respectively; iii) at 0.9 V, the dominant species are the 1.75 eru species.

2.6. Inversion of the Seebeck Coefficient

To further elucidate the mechanisms of charge transport in this polymer model system, we measured the Seebeck coefficient of electrochemically doped BBL. In order to minimize the effect of gate current leakage, we again allowed the gel electrolyte to partially dry under ambient conditions. The results of the thermoelectric measurements are summarized in **Figure 5**A. Note that we could measure the thermovoltage reliably only in the gate voltage range 0.15–0.75 V due to the reduced conductivity of BBL outside this range. We observe a sign change in the Seebeck coefficient (S) occurring at about the same doping concentration at which the conductivity σ reaches a maximum (i.e., at 0.5 V or ≈0.68 eru). Importantly, the charged states in Figure 5A correlate well with our electrical, optical (UV–vis–NIR), vibrational (Raman), magnetic (EPR), and DFT characterizations. Specifically, the conductivity decrease for gate voltages larger than 0.5 V coincides with the observation of multiply charged states, associated with large doping levels ranging from 0.75 to 1.75 eru in the UV–vis and Raman spectra, and the saturation of the spin density in EPR.

The Seebeck coefficient is proportional to the difference between the Fermi level and the transport energy level, which can be expressed as[27]

$$S = \frac{k_B}{q}\frac{E^* - E_F}{k_B T} \quad (1)$$

where k_B is the Boltzmann constant, q is the elemental charge, T is the absolute temperature, E_F is the Fermi level under

© 2022 The Authors. Advanced Functional Materials published by Wiley-VCH GmbH

16163028, 2022, 20, Downloaded from https://onlinelibrary.wiley.com/doi/10.1002/adfm.202112276 by Area Sistemi Dipart & Document, Wiley Online Library on [23/11/2022]. See the Terms and Conditions (https://onlinelibrary.wiley.com/terms-and-conditions) on Wiley Online Library for rules of use; OA articles are governed by the applicable Creative Commons License

16163028, 2022, 20, Downloaded from https://onlinelibrary.wiley.com/doi/10.1002/adfm.202112276 by Area Sistemi Dipart & Document, Wiley Online Library on [23/11/2022]. See the Terms and Conditions (https://onlinelibrary.wiley.com/terms-and-conditions) on Wiley Online Library for rules of use; OA articles are governed by the applicable Creative Commons License

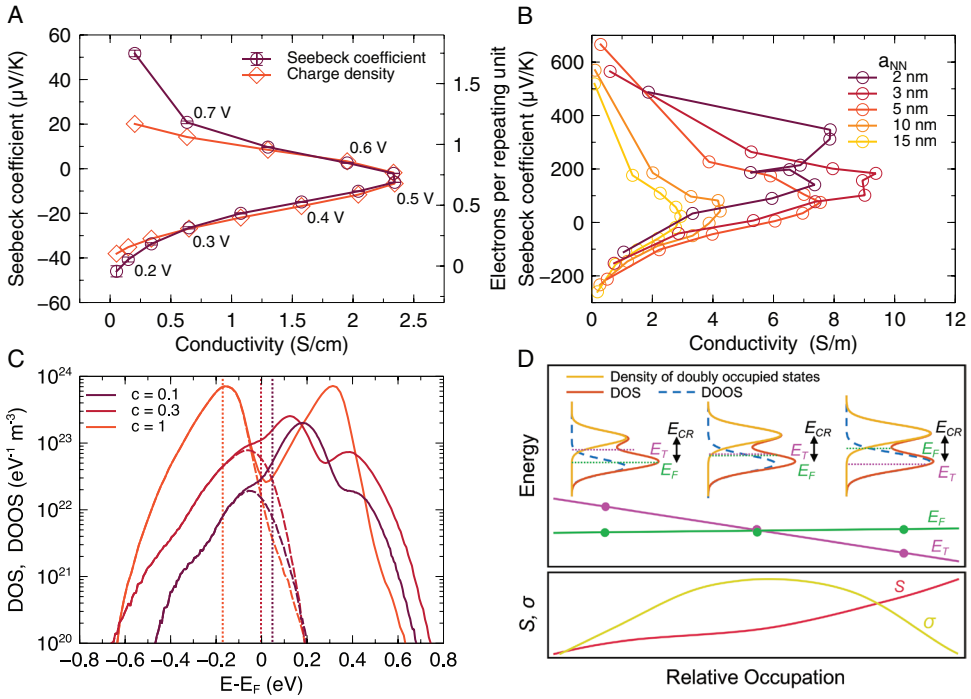

Figure 5. Experimental and Monte-Carlo simulations of the relation between Seebeck coefficient and conductivity in electrochemically doped BBL. A) Seebeck coefficient and charge density (electrons per repeating unit) as a function of conductivity of a BBL-based OECT with a partially dried PSSNa gel electrolyte. B) Seebeck coefficient versus electrical conductivity for different lattice constants a_{NN}. The Seebeck coefficient and electrical conductivity versus relative occupation are illustrated in Figure S10 in the Supporting Information. C) Calculated DOS (solid lines) and DOOS (dashed lines) with respect to the Fermi energy for relative occupations of 0.1, 0.3, and 1 at a_{NN} = 3 nm. D) Schematics of the DOS, DOOS, and relation to energetics and conductivity with increasing relative occupation.

certain doping level, and E^* is the transport energy level, which is defined as

$$E^* = \int \frac{E\,\sigma(E)}{\sigma}\,\mathrm{d}E \tag{2}$$

where $\sigma(E)$ is the conductivity distribution function and $\sigma = \int \sigma(E)\,\mathrm{d}E$ is the total conductivity that, according to percolation theory, is roughly proportional to $\sigma \propto \exp(-|E^* - E_F|/k_BT)$. Hence, the Seebeck coefficient reflects the relative positions between the Fermi and transport levels, and a conductivity maximum is therefore expected when S changes sign. For n-type conducting polymers with low doping concentration, the Fermi level sits at the tail of DOS while the transport energy level lies closer to the peak of the DOS, resulting in a negative Seebeck coefficient. Since, at low and intermediate charge carrier concentrations, the transport energy only depends on the shape and width of the DOS while the Fermi energy increases with doping concentration, the absolute value of the Seebeck coefficient decreases while the electrical conductivity increases. In a recent study, Zeng et al.[28] proposed such a simple state filling model for the case of band transport and noninteracting charges to describe the sign change of the Seebeck coefficient in a $FeCl_3$ doped diketopyrrolopyrrole based donor–acceptor copolymer. In Figure S8 in the Supporting Information, we show that also in the case of hopping transport such a model can, at least phenomenologically, describe the high-doping level data shown in Figure 5A. However, it fails to describe the observed multiple occupation effects, cf. Figure 1. Moreover, the small mean distance between charges at the doping levels at hand leads to Coulomb energies in the order of 10–100 meV that are not small compared to the other relevant energies in the system (k_BT = 25 meV, disorder 50–100 meV) and hence cannot be ignored.

2.7. Kinetic Monte Carlo Simulations

In the following, we therefore use numerically exact kinetic Monte Carlo (kMC) simulations to model the data in Figure 5A. In short, the simulations are carried out by a kMC model for Coulombically interacting particles hopping on a cubic lattice (lattice constant a_{NN}) with an exponential DOS. The latter is chosen to account for the fact that at the high dopant densities that are relevant here, the Coulomb potentials from the ionized dopants produce a dominant exponential tail in the DOS.[29] Further details are given in ref. [30] and Figure S9 in the Supporting Information, where we also show that the key conclusions from the kMC model do not depend on the shape of the original DOS. Figure 5b shows the calculated Seebeck coefficient as a function of the electrical conductivity for different lattice constants with relative occupation (charges per site) ranging from 10% to 100%. The Seebeck coefficient and conductivity versus relative occupation are shown in Figure S10 in the Supporting Information. The electrical conductivity and Seebeck coefficient demonstrate the same pattern as the experimental data.

© 2022 The Authors. Advanced Functional Materials published by Wiley-VCH GmbH

16163028, 2022, 20, Downloaded from https://onlinelibrary.wiley.com/doi/10.1002/adfm.202112276 by Area Sistemi Dipart & Document, Wiley Online Library on [23/11/2022]. See the Terms and Conditions (https://onlinelibrary.wiley.com/terms-and-conditions) on Wiley Online Library for rules of use; OA articles are governed by the applicable Creative Commons License

The observed behavior can be understood from the evolution of the shape of the DOS at high doping levels as schematically illustrated in Figure 5D. Above the original DOS, a second peak appears that reflects the DOS available for double occupation. This peak is a clone of the density of occupied states (DOOS), shifted toward higher energies by the Coulomb repulsion energy (E_{CR}), that roughly equals the interaction strength between two charge carriers occupying a single site (0.5 eV in the simulations). Once the Fermi energy approaches the lower tail of this second peak (left image of Figure 5D), double occupation will set in. In this regime, the transport energy is still above E_F, and S remains negative. Around unity occupation (right image), the areas of the two peaks in the DOS are equal and the Fermi energy lies in the gap region. Here, charge transport is no longer dominated by excitations from occupied states around E_F to empty states above E_F, but by excitations from occupied states below E_F to available states around E_F that are then doubly occupied. Equivalently, this regime may be described as the excitation of holes, that in this case correspond to singly occupied states around the Fermi energy, to the transport level where most sites are doubly occupied. In both cases, the transport energy lies below E_F and S is positive. The middle panel in Figure 5D shows the intermediate case where E_F and E^* coincide, S changes sign and σ peaks.

The kMC-calculated DOS and DOOS are plotted with respect to the Fermi energy in Figure 5C. Despite the additional broadening of the DOS caused by the Coulomb interactions, the calculations show the same behavior as sketched in Figure 5D. By increasing the relative occupation, the transport energy approaches the Fermi energy and crosses it at a relative occupation of 30%, in reasonable agreement to the experimental data. At a relative occupation of 100%, the Fermi energy lies in the gap between the first and the second peak of the DOS and the system behaves like a Mott–Hubbard insulator system.

In a recent study by Liu et al.[14] the decrease in the electrical conductivity upon increasing the dopant concentration was attributed to the formation of a soft Coulomb gap as described by the Efros–Shklovskii theory. While our results indicate that the sign change in S is the result of the opening of a hard Coulomb gap, the reduction in the electrical conductivity is due to a combined effect of both the soft and hard Coulomb gaps. Upon closer inspection, the DOS for relative occupations of 0.1 and 0.3 in Figure 5C show a slight reduction around the Fermi energy that can be attributed to formation of a soft Coulomb gap at the Fermi energy. The effect of the formation of an (incomplete) soft Coulomb gap can be seen in Figure 5B as a dip in the conductivity around the conductivity maximum. As expected on basis of the ES theory, the effect becomes more pronounced for larger (unperturbed) DOS, i.e., for the smaller lattice constants of 2 and 3 nm.

Comparing the simulated curves in Figure 5B to the experimental data in Figure 5A suggests that values for a_{NN} of around 3–5 nm are most representative for the system. As this is significantly larger than the monomer size of ≈1 nm, this raises a question to the physical meaning of a_{NN}. The most straightforward interpretation is that a_{NN} reflects a typical aggregate size, i.e., the rate limiting steps in the charge transport are hops between aggregates. Interestingly, aggregate sizes in the range $(3–5)^3$ nm^3 match well to the values extracted from GIWAXS of pristine BBL: the (010) π–π stacking coherence length is about 35 Å, while the (100) coherence length is a bit less than 20 Å.[31] Furthermore, a polaron is primarily delocalized over three monomer units in a BBL chain,[16] indicating that the coherence lengths and polaron delocalization length match extremely well with our estimated range for the unit cell size.

3. Conclusion

In summary, we studied the charge transport dynamics of the electrochemically doped polymer model system BBL. The electrical conductivity of BBL reaches a maximum value of 3.1 S cm^{-1} at a doping level of 0.7 electrons per repeating unit and then decreases to a nearly nonconductive state at higher doping levels. In situ EPR, UV–vis–NIR and Raman spectroelectrochemistry, in combination with DFT/TD-DFT calculations, corroborate the formation of multiply charged species with reduced mobility at high doping levels. To further study the charge transport mechanism in BBL, we measured the Seebeck coefficient at different charge densities and observed Seebeck polarity inversion from n-type to p-type, although the polymer itself was negatively charged. The sign change of the Seebeck coefficient occurred at the same doping level the conductivity reached the maximum value. We employed kinetic Monte Carlo simulations to elucidate the underlying mechanisms, with both Coulomb repulsion and double occupation considered in the model. Our kMC simulations showed a similar trend as the experimental data suggesting that the inversion of the Seebeck coefficient, which coincides with the maximum in electrical conductivity, is caused by filling of the density of states and opening of a hard Coulomb gap around the Fermi energy. We also postulated that the previously proposed soft Efros–Shklovskii Coulomb gap[14] is of minor importance, at least for the highly planar and rigid BBL polymer investigated here. Our results provide a simple picture that clarifies the general observation of Seebeck coefficient inversion and electrical conductivity drop in highly doped conducting polymers and have implications for the rational design of high-performance organic thermoelectric materials and electrochemically active mixed ion-electron conductors.

4. Experimental Section

Sample Fabrication: High-molecular weight BBL (η = 11.6 dL g^{-1} in methanesulfonic acid (MSA) at 30 °C, M_w = 60.5 kDa) was stirred overnight to fully dissolve in MSA at a concentration of 5 mg mL^{-1}. The films of BBL were fabricated by spin coating onto glass or PET substrates with a spin rate of 1000 RPM, followed by dipping the wet film briefly into IPA and deionized water for at least 3 h to remove residual MSA. The BBL film was dried by blowing with nitrogen gas. The film thickness was ≈ 60 nm in all cases.

Electrical Characterization: OECTs were prepared by thermally evaporating 3/30 nm Cr/Au as electrodes before BBL deposition. The channel length of the devices was 0.5 mm and the channel width was 10 mm. The composition of the PSSNa gel was PSSNa/D-Sorbitol/glycerol/deionized water at 40/10/10/40 wt%. The electrolyte was doctor bladed on top of the BBL film and a Ag/AgCl pellet was used as the gate electrode in all cases. To measure the Seebeck coefficient a pair of Peltier modules were used to provide a temperature gradient, followed by measuring the open voltage between the source and drain contacts

© 2022 The Authors. Advanced Functional Materials published by Wiley-VCH GmbH

16163028, 2022, 20, Downloaded from https://onlinelibrary.wiley.com/doi/10.1002/adfm.202112276 by Area Sistemi Dipart & Document, Wiley Online Library on [23/11/2022]. See the Terms and Conditions (https://onlinelibrary.wiley.com/terms-and-conditions) on Wiley Online Library for rules of use; OA articles are governed by the applicable Creative Commons License

(Figure S11, Supporting Information). To minimize the gate leakage current, the PSSNa gel was partially dried under ambient conditions (40 RH%) resulting in the water content of the polyelectrolyte decreasing from 40 to 12 wt% as determined by mass loss in the gel electrolyte. The reduction in water content also acts to largely suppress ionic conductivity and allows to measure the electronic Seebeck coefficient of BBL, as supported by the stability of the open voltage and lack of ionic Seebeck coefficient transients in the measurement shown in Figure S11B in the Supporting Information. To estimate the charge density, we measured the BBL film density using a Quartz Crystal Microbalance with Dissipation monitoring (QCM-D, Q-Sense by Biolin Scientific). The charge density (electrons per repeating unit) at different gate voltages was then calculated using the method shown in Figure S2B in the Supporting Information.

UV–vis–NIR Spectroscopy: UV–vis–NIR difference spectra were measured in reflectance mode using an Avantes Avaspec-ULS-2048L fiber optic spectrometer coupled with an Avalight-HAL-S-Mini halogen light source. The light source and spectrometer were connected to a fiber optic reflectance probe to which the light beam reflected from the Au substrate below the BBL layer. UV–vis microspectroscopy in transmission mode were measured using an Ocean Insight QE Pro spectrometer coupled to a Nikon Eclipse L200N optical microscope. The beam size collected by the spectrometer from the sample was ≈40 µm in diameter. Spectra measured from different positions inside the OECT channel are shown in Figure S12A in the Supporting Information.

Raman Spectroscopy: Raman measurements were performed with a Raman system integrated in an inverted microscope (Nikon Ti-E) with a 60× air objective (Nikon, NA = 0.7). A 532 nm DPSS laser (λ-beam, RGB Photonics) was used for excitation with the output power set to 5 mW. A spectrograph (Andor Kymera 328i) with a 600 l mm^{-1} diffraction grating (blazed at 500 nm) was used for analysis. The signal was collected with a thermoelectrically cooled EMCCD camera (–80 °C, Andor Newton DU970P-BVF). Five images, each integrated for 10 s, were used for every spectrum. The spectra for spectroelectrochemical characterization were collected in the same focal point under different applied voltages. Spectra measured from different positions inside the OECT channel are shown in Figure S12B in the Supporting Information. A bipolynomial Matlab code baseline subtraction was applied to the measured raw data.

EPR Measurements: The samples for EPR measurements were prepared on PET substrates with 20 nm Au contacts, followed by coating a thin layer of electrolyte on top of BBL. The Ag/AgCl gate electrode was placed outside of the resonance chamber during the measurements. The sample size was about 2 mm by 20 mm. The EPR spectra were measured after allowing the drain current to stabilize for at least 1 min under the applied gate voltage to ensure that the film was fully doped.

DFT Calculations: Details of the DFT and TD-DFT calculations are reported in the Supporting Information.

Supporting Information

Supporting Information is available from the Wiley Online Library or from the author.

Acknowledgements

K.X. and T.-P.R. contributed equally to this work. This work was financially supported by the Swedish Research Council (2020-03243), Olle Engkvists Stiftelse (204-0256), the European Commission through the Marie Sklodowska-Curie projects HORATES (GA-955837), and the project HyThermEl (GA-799477), the Swedish Government Strategic Research Area in Materials Science on Functional Materials at Linköping University (Faculty Grant SFO-Mat-LiU 2009-00971), and the Deutsche Forschungsgemeinschaft (DFG, German Research Foundation) under Germany's Excellence Strategy via the Excellence Cluster 3D Matter Made to Order (EXC-2082/1-390761711). M.K. thanks the Carl Zeiss Foundation for financial support. D.F. acknowledges the Deutsche Forschungsgemeinschaft for the grant FA 1502/1-1 "Molecular Understanding of Thermo-Electric Properties in Organic Polymers" and the Regional Computing Centre (RRZK) of Universitaet zu Koeln, for providing computing time and resources on the HPC RRZK CHEOPS. H.S. acknowledges support from the National Natural Science Foundation of China (Grant No. 52173156). J.S.M.F., J.O.P., and T.E. were supported by the Swedish Foundation for Strategic Research (ITM17-0316).

Conflict of Interest

The authors declare no conflict of interest.

Data Availability Statement

The data that support the findings of this study are available from the corresponding author upon reasonable request.

Keywords

conducting polymers, organic electrochemical transistor, Seebeck coefficient, thermoelectric application

Received: December 1, 2021
Revised: January 19, 2022
Published online: February 5, 2022

[1] a) X. Guo, A. Facchetti, *Nat. Mater.* **2020**, *19*, 922; b) T. Someya, Z. Bao, G. G. Malliaras, *Nature* **2016**, *540*, 379.

[2] a) T. Sekitani, H. Nakajima, H. Maeda, T. Fukushima, T. Aida, K. Hata, T. Someya, *Nat. Mater.* **2009**, *8*, 494; b) H. Zheng, Y. Zheng, N. Liu, N. Ai, Q. Wang, S. Wu, J. Zhou, D. Hu, S. Yu, S. Han, W. Xu, C. Luo, Y. Meng, Z. Jiang, Y. Chen, D. Li, F. Huang, J. Wang, J. Peng, Y. Cao, *Nat. Commun.* **2013**, *4*, 1971.

[3] a) S. Holliday, R. S. Ashraf, A. Wadsworth, D. Baran, S. A. Yousaf, C. B. Nielsen, C.-H. Tan, S. D. Dimitrov, Z. Shang, N. Gasparini, M. Alamoudi, F. Laquai, C. J. Brabec, A. Salleo, J. R. Durrant, I. McCulloch, *Nat. Commun.* **2016**, *7*, 11585; b) X. Guo, N. Zhou, S. J. Lou, J. Smith, D. B. Tice, J. W. Hennek, R. P. Ortiz, J. T. L. Navarrete, S. Li, J. Strzalka, L. X. Chen, R. P. H. Chang, A. Facchetti, T. J. Marks, *Nat. Photonics* **2013**, *7*, 825.

[4] a) D. Moia, A. Giovannitti, A. A. Szumska, I. P. Maria, E. Rezasoltani, M. Sachs, M. Schnurr, P. R. F. Barnes, I. McCulloch, J. Nelson, *Energy Environ. Sci.* **2019**, *12*, 1349; b) A. V. Volkov, H. Sun, R. Kroon, T.-P. Ruoko, C. Che, J. Edberg, C. Muller, S. Fabiano, X. Crispin, *ACS Appl. Energy Mater.* **2019**, *2*, 5350; c) H. Wang, Y. Diao, Y. Lu, H. Yang, Q. Zhou, K. Chrulski, J. M. D'Arcy, *Nat. Commun.* **2020**, *11*, 3882.

[5] a) M. Massetti, F. Jiao, A. J. Ferguson, D. Zhao, K. Wijeratne, A. Würger, J. L. Blackburn, X. Crispin, S. Fabiano, *Chem. Rev.* **2021**, *121*, 12465; b) B. Russ, A. Glaudell, J. J. Urban, M. L. Chabinyc, R. A. Segalman, *Nat. Rev. Mater.* **2016**, *1*, 16050; c) R. Kroon, D. A. Mengistie, D. Kiefer, J. Hynynen, J. D. Ryan, L. Yu, C. Müller, *Chem. Soc. Rev.* **2016**, *45*, 6147; d) X. Zhao, D. Madan, Y. Cheng, J. Zhou, H. Li, S. M. Thon, A. E. Bragg, M. E. DeCoster, P. E. Hopkins, H. E. Katz, *Adv. Mater.* **2017**, *29*, 1606928.

[6] a) D. Ohayon, G. Nikiforidis, A. Savva, A. Giugni, S. Wustoni, T. Palanisamy, X. Chen, I. P. Maria, E. Di Fabrizio, P. M. F. J. Costa,

© 2022 The Authors. Advanced Functional Materials published by Wiley-VCH GmbH

I. McCulloch, S. Inal, *Nat. Mater.* **2020**, *19*, 456; b) E. Zeglio, A. L. Rutz, T. E. Winkler, G. G. Malliaras, A. Herland, *Adv. Mater.* **2019**, *31*, 1806712; c) H. Li, W. Shi, J. Song, H.-J. Jang, J. Dailey, J. Yu, H. E. Katz, *Chem. Rev.* **2019**, *119*, 3.

[7] a) P. Gkoupidenis, D. A. Koutsouras, G. G. Malliaras, *Nat. Commun.* **2017**, *8*, 15448; b) E. J. Fuller, S. T. Keene, A. Melianas, Z. Wang, S. Agarwal, Y. Li, Y. Tuchman, C. D. James, M. J. Marinella, J. J. Yang, A. Salleo, A. A. Talin, *Science* **2019**, *364*, 570; c) J. Y. Gerasimov, R. Gabrielsson, R. Forchheimer, E. Stavrinidou, D. T. Simon, M. Berggren, S. Fabiano, *Adv. Sci.* **2019**, *6*, 1801339; d) X. Ji, B. D. Paulsen, G. K. K. Chik, R. Wu, Y. Yin, P. K. L. Chan, J. Rivnay, *Nat. Commun.* **2021**, *12*, 2480.

[8] I. Salzmann, G. Heimel, M. Oehzelt, S. Winkler, N. Koch, *Acc. Chem. Res.* **2016**, *49*, 370.

[9] a) D. Kiefer, R. Kroon, A. I. Hofmann, H. Sun, X. Liu, A. Giovannitti, D. Stegerer, A. Cano, J. Hynynen, L. Yu, Y. Zhang, D. Nai, T. F. Harrelson, M. Sommer, A. J. Moule, M. Kemerink, S. R. Marder, I. McCulloch, M. Fahlman, S. Fabiano, C. Muller, *Nat. Mater.* **2019**, *18*, 149; b) X. Zhao, D. Madan, Y. Cheng, J. Zhou, H. Li, S. M. Thon, A. E. Bragg, M. E. DeCoster, P. E. Hopkins, H. E. Katz, *Adv. Mater.* **2017**, *29*, 1606928; c) C. G. Tang, M. N. Syafiqah, Q.-M. Koh, C. Zhao, J. Zaini, Q.-J. Seah, M. J. Cass, M. J. Humphries, I. Grizzi, J. H. Burroughes, R.-Q. Png, L.-L. Chua, P. K. H. Ho, *Nature* **2019**, *573*, 519; d) H. Guo, C.-Y. Yang, X. Zhang, A. Motta, K. Feng, Y. Xia, Y. Shi, Z. Wu, K. Yang, J. Chen, Q. Liao, Y. Tang, H. Sun, H. Y. Woo, S. Fabiano, A. Facchetti, X. Guo, *Nature* **2021**, *599*, 67.

[10] a) K. Xu, H. Sun, T. P. Ruoko, G. Wang, R. Kroon, N. B. Kolhe, Y. Puttisong, X. Liu, D. Fazzi, K. Shibata, C. Y. Yang, N. Sun, G. Persson, A. B. Yankovich, E. Olsson, H. Yoshida, W. M. Chen, M. Fahlman, M. Kemerink, S. A. Jenekhe, C. Muller, M. Berggren, S. Fabiano, *Nat. Mater.* **2020**, *19*, 738; b) C.-Y. Yang, M.-A. Stoeckel, T.-P. Ruoko, H.-Y. Wu, X. Liu, N. B. Kolhe, Z. Wu, Y. Puttisong, C. Musumeci, M. Massetti, H. Sun, K. Xu, D. Tu, W. M. Chen, H. Y. Woo, M. Fahlman, S. A. Jenekhe, M. Berggren, S. Fabiano, *Nat. Commun.* **2021**, *12*, 2354.

[11] J. D. Yuen, A. S. Dhoot, E. B. Namdas, N. E. Coates, M. Heeney, I. McCulloch, D. Moses, A. J. Heeger, *J. Am. Chem. Soc.* **2007**, *129*, 14367.

[12] M. Fahlman, S. Fabiano, V. Gueskine, D. Simon, M. Berggren, X. Crispin, *Nat. Rev. Mater.* **2019**, *4*, 627.

[13] S. Hwang, W. J. Potscavage, Y. S. Yang, I. S. Park, T. Matsushima, C. Adachi, *Phys. Chem. Chem. Phys.* **2016**, *18*, 29199.

[14] J. Liu, G. Ye, B. V. Zee, J. Dong, X. Qiu, Y. Liu, G. Portale, R. C. Chiechi, L. J. A. Koster, *Adv. Mater.* **2018**, *30*, 1804290.

[15] Z. Liang, H. H. Choi, X. Luo, T. Liu, A. Abtahi, U. S. Ramasamy, J. A. Hitron, K. N. Baustert, J. L. Hempel, A. M. Boehm, A. Ansary, D. R. Strachan, J. Mei, C. Risko, V. Podzorov, K. R. Graham, *Nat. Mater.* **2021**, *20*, 518.

[16] S. Wang, H. Sun, U. Ail, M. Vagin, P. O. Persson, J. W. Andreasen, W. Thiel, M. Berggren, X. Crispin, D. Fazzi, S. Fabiano, *Adv. Mater.* **2016**, *28*, 10764.

[17] a) H. Sun, J. Gerasimov, M. Berggren, S. Fabiano, *J. Mater. Chem. C* **2018**, *6*, 11778; b) H. Sun, M. Vagin, S. Wang, X. Crispin, R. Forchheimer, M. Berggren, S. Fabiano, *Adv. Mater.* **2018**, *30*, 1704916.

[18] P. Andersson Ersman, D. Nilsson, J. Kawahara, G. Gustafsson, M. Berggren, *Org. Electron.* **2013**, *14*, 1276.

[19] B. Wang, A. J. Fielding, R. A. W. Dryfe, *Chem. Commun.* **2018**, *54*, 3827.

[20] J. H. Freed, G. K. Fraenkel, *J. Chem. Phys.* **1963**, *39*, 326.

[21] R. C. Barklie, M. Collins, S. R. P. Silva, *Phys. Rev. B* **2000**, *61*, 3546.

[22] a) D. Fazzi, S. Fabiano, T.-P. Ruoko, K. Meerholz, F. Negri, *J. Mater. Chem. C* **2019**, *7*, 12876; b) D. Fazzi, F. Negri, *Adv. Electron. Mater.* **2020**, *7*, 2000786.

[23] a) C. M. Marian, A. Heil, M. Kleinschmidt, *Wiley Interdiscip. Rev.: Comput. Mol. Sci.* **2018**, *9*, e1394; b) D. Maganas, S. DeBeer, F. Neese, *J. Phys. Chem. A* **2018**, *122*, 1215; c) P. Norman, A. Dreuw, *Chem. Rev.* **2018**, *118*, 7208.

[24] S. Grimme, A. Hansen, *Angew. Chem., Int. Ed.* **2015**, *54*, 12308.

[25] A. C. Albrecht, *J. Chem. Phys.* **1961**, *34*, 1476.

[26] C. Francis, D. Fazzi, S. B. Grimm, F. Paulus, S. Beck, S. Hillebrandt, A. Pucci, J. Zaumseil, *J. Mater. Chem. C* **2017**, *5*, 6176.

[27] H. Abdalla, *Doctoral Thesis*, Linköping University, xxxx **2018**.

[28] H. Zeng, M. Mohammed, V. Untilova, O. Boyron, N. Berton, P. Limelette, B. Schmaltz, M. Brinkmann, *Adv. Electron. Mater.* **2021**, *7*, 2000880.

[29] M. Silver, L. Pautmeier, H. Bässler, *Solid State Commun.* **1989**, *72*, 177.

[30] G. Zuo, H. Abdalla, M. Kemerink, *Phys. Rev. B* **2016**, *93*, 235203.

[31] H. Y. Wu, C. Y. Yang, Q. Li, N. B. Kolhe, X. Strakosas, M. A. Stoeckel, Z. Wu, W. Jin, M. Savvakis, R. Kroon, D. Tu, H. Y. Woo, M. Berggren, S. A. Jenekhe, S. Fabiano, *Adv. Mater.* **2022**, *34*, 2106235.

© 2022 The Authors. Advanced Functional Materials published by Wiley-VCH GmbH

16163028, 2022, 20, Downloaded from https://onlinelibrary.wiley.com/doi/10.1002/adfm.202112276 by Area Sistemi Dipart & Document, Wiley Online Library on [23/11/2022]. See the Terms and Conditions (https://onlinelibrary.wiley.com/terms-and-conditions) on Wiley Online Library for rules of use; OA articles are governed by the applicable Creative Commons License